Micro-alloying of Zn and Ca in vacuum induction casted bioresorbable Mg system: Perspectives on corrosion resistance, cytocompatibility, and inflammatory response

Manisha Behera, Agnes Denys, Rajashekhara Shabadi, Fabrice Allain, Cosmin Gruescu

KeAi
CHINESE ROOTS
GLOBAL IMPACT

Available online at www.keaipublishing.com/en/journals/journal-of-magnesium-and-alloys/

ScienceDirect

Journal of Magnesium and Alloys 12 (2024) 2812–2825

www.elsevier.com/locate/jma

Full Length Article

Micro-alloying of Zn and Ca in vacuum induction casted bioresorbable Mg system: Perspectives on corrosion resistance, cytocompatibility, and inflammatory response

Manisha Behera[a], Agnès Denys[b], Rajashekhara Shabadi[a,*], Fabrice Allain[b], Cosmin Gruescu[a]

[a] *Unité Matériaux et Transformations (UMET), Université de Lille, CNRS, INRA, ENSCL, UMR 8207, UMET, F-59000 Lille, France*
[b] *Université de Lille, CNRS, UMR 8576 - UGSF - Unité de Glycobiologie Structurale et Fonctionnelle, F-59000 Lille, France*

Received 9 March 2024; received in revised form 13 June 2024; accepted 2 July 2024
Available online 26 July 2024

Abstract

There is an increasing interest in biodegradable materials, such as magnesium, for orthopaedic implants. This is driven by their potential to address challenges like stress shielding and the need for secondary removal surgery. In this study, biodegradable magnesium alloys were produced using the Vacuum Induction Casting technique. The impact of micro-alloying Zn and Ca in Mg–*x*Zn–0.2Ca (x = 0.1, 0.2, 0.3, and 0.4 wt%) alloys on corrosion resistance, cytocompatibility, and early-stage inflammatory response was investigated. XRD and SEM-EDS analysis confirmed the presence of $Ca_2Mg_6Zn_3$ secondary phases in all alloys. The Mg–0.3Zn–0.2Ca alloy exhibited the lowest corrosion rate and an elastic modulus of 36.8 GPa, resembling that of natural bone. Electrochemical measurements indicated a correlation between grain size and secondary phase volume fraction in explaining corrosion behaviour. In vitro degradation in simulated body fluid (SBF) for 21 days showed hydroxyapatite formation on alloy surfaces, aligning with electrochemical studies. In vitro cytotoxicity tests demonstrated the cytocompatibility of all alloys, with Mg–0.3Zn–0.2Ca having the highest cell viability over a 6-day cell culture. Investigation into the inflammatory response with RAW-Blue macrophages revealed the anti-inflammatory properties of Mg–0.3Zn–0.2Ca alloys. Micro-alloying with 0.3 wt% Zn and 0.2 wt% Ca enhanced mechanical properties, corrosion resistance, cytocompatibility, and immunomodulatory properties. This positions the Mg–0.3Zn–0.2Ca alloy as a promising biodegradable implant for bone fixation applications.

Keywords: Micro-alloying; MgZnCa; Corrosion resistance; In vitro; Anti-inflammatory response.

1. Introduction

Corrosion susceptibility of biodegradable Magnesium (Mg) alloys in physiological Chlorine environment is a major limitation for its clinical applicability [1]. Magnesium as biomedical implant has numerous advantages due to its density, mechanical strength, and elastic modulus close to the natural bone properties [1]. Mg is one of the most important bivalent ions associated with the formation of the biological apatite and shows direct influence on bone metabolism [2]. Alloying with elements like Al, Li, or Co has been reported to enhance the corrosion resistance of the Mg alloys. However, introducing these elements in the implant system could lead to chronic cytotoxic responses in the host system [3,4]. For example, the presence of aluminium exerts neurotoxic effects due to the generation of reactive oxygen species (ROS) and free radicals [5]. Similar toxic responses were reported in the past for Li [6] and Co [7]. Therefore, developing Mg alloys with physiologically present elements like Zinc (Zn) and Calcium (Ca), as bio-implants could be a desirable solution [8].

Several studies proposed Al and Rare Earth elements free Mg alloys like Mg–Ca [9] and Mg-Zn [10]. The addition of Ca enhances ductility, while zinc improves corrosion resistance. The combination of these elements, calcium, and zinc, has been observed to refine grain structure and enhance

* Corresponding author.
E-mail address: rajashekhara.shabadi@univ-lille.fr (R. Shabadi).

https://doi.org/10.1016/j.jma.2024.07.001

mechanical properties [11]. Similarly, the addition of other elements like Mn and Si can result in mechanically improved alloy system although they have not undergone evaluations for cytotoxicity [12]. However, the alloying concentration of Zn and Ca along with the Zn/Ca atomic ratio influence significantly to the corrosion resistance and mechanical properties of the alloy system [13,14]. Based on previous reports, if the concentration of Zn > 2 wt% and concentration of Ca > 1 wt%, extensive formation of secondary precipitates like $Ca_2Mg_6Zn_3$ and Mg_2Ca was observed [15–17]. An ideal biomaterial should be devoid of any kind of secondary phases or precipitates [18] to prevent the galvanic coupling between the precipitates and the α-Mg matrix [19,20].

Micro-alloying of Zn and Ca into Mg matrix in a trace amount (i.e., 1 wt%) could be an effective way to improve the mechanical properties with reduced secondary phases [21]. Elemental addition of both Zn and Ca is more effective in altering the microstructure and mechanical properties of Mg alloys as compared to their individual addition in trace amounts [22–24]. These alloying elements enhance the corrosion behaviour of Mg but evaluating the influence of these corrosion products on cellular activity is an important step toward the acceptance of Mg-based materials for bio-medical orthopaedic applications. Material cytotoxicity or other biological tests are performed using the cells of target tissue such as osteoblast cells for musculoskeletal applications [25]. Along with cytocompatibility, biodegradable materials should have intrinsic ability to direct an immune response for better implant integration, while avoiding any chronic inflammation or foreign body reactions [26]. Macrophages are the immunological cells that balance the acute and chronic inflammation via cytokine release. Hence cytocompatibility, macrophage fusion, and cytokine release influence tissue healing and remodelling, further affecting biomaterial properties and performance [27,28].

In this study, we used micro-alloying of Zinc and Calcium in Magnesium via Vacuum Induction casting technique to elucidate the evolution of secondary phases and their correlation with mechanical and corrosion properties in Mg alloys. To assess biological significance, we evaluated the cytocompatibility of four as-cast Mg–*x*Zn–0.2Ca (x = 0.1, 0.2, 0.3, and 0.4 wt%) alloys according to ISO standards, using indirect cell culture with MC3T3-E1 cells in vitro. Additionally, we conducted lipopolysaccharide (LPS)-induced early-stage inflammatory response assays on the most cytocompatible Mg–*x*Zn–0.2Ca alloys with RAW-Blue cells in vitro to investigate their anti-inflammatory properties. This paper is the first of its kind, providing a comprehensive approach from the initial conception of the alloy to its biological evaluation.

2. Materials and methods

2.1. Material fabrication

Four Magnesium alloys with varying amounts of Zn (x = 0.1, 0.2, 0.3, and 0.4 wt%) and 0.2 wt% Ca were prepared by melting a combination of commercial pure Mg (99.95 %), Mg-30 wt% Zn master alloy, and Mg-22 wt% Ca master alloy. Table 1 presents the nomenclature and nominal composition of all the alloys. Relevant alloy compositions concerning their mass percentages were melted in a graphite crucible inside a Vacuum Induction Casting equipment (Indutherm VC 480) maintained under a pure Argon (Ar) atmosphere. Prior to melting, both melting and casting chambers were purged with ultra-high purity Ar and maintained under Ar atmosphere to prevent oxidation of the molten metal. The melting pressure was adjusted to 0.5 bar to initiate heating. The temperature was progressively raised to 690 °C while maintaining continuous electromagnetic-induced agitation to ensure proper mixing. Upon complete melting, the molten alloy was poured into a steel mold preheated to 400 °C. The casting pressure was the same as the melting pressure. The alloys were cooled completely inside the casting chamber. For the metallographic studies, standard procedures such as mechanical grinding up to 4000 grit, diamond polishing until 0.25μm mirror finish, and ultrasonically cleaning in absolute ethanol and then drying in hot air, before material characterization.

Table 1
Nomenclature and nominal composition of as-cast Mg alloys.

Nomenclature	Material condition	Nominal composition (by wt%)
CZ00	As-cast	Commercially pure magnesium (99.99 %)
CZ01	As-cast	Mg 99.7 %, Zn 0.1 %, Ca 0.2 %
CZ02	As-cast	Mg 99.6 %, Zn 0.2 %, Ca 0.2 %
CZ03	As-cast	Mg 95.5 %, Zn 0.3 %, Ca 0.2 %
CZ04	As-cast	Mg 99.4 %, Zn 0.4 %, Ca 0.2 %

2.2. Scanning electron microscopy and X-ray diffraction

In-depth microstructural analysis of the alloys was investigated using Hitachi SU 5000 Scanning Electron Microscope (SEM) equipped with Energy Dispersive X-Ray spectrometer (EDS) for the analysis of secondary phases. Further, phase analysis of Mg alloys was carried out using Rigaku X-Ray diffractometer with CuK_α radiation as an excitation source. Samples were scanned from 2Θ range of 5° to 80° with a scan speed of 0.02° s^{-1}. XRD peak analysis was done using Diffrac.Eva(Bruker) software and matched with respective ICDD databases.

2.3. Microstructural characterisation

The samples polished upto 0.25 μm surface finish were chemically etched with Acetic-Picral solution to observe the grain morphology and microstructure of the alloys in optical microscope (Olympus). The unetched samples were observed in SEM with Back-Scattered Electron (BSE) mode to distinguish different atomic phases.

2.4. Mechanical properties

The mechanical properties of the alloys were evaluated using uniaxial tensile test performed on miniature tensile spec-

imens with overall length of 30 mm, fillet radius of 2 mm, gauge length of 12 mm, width and thickness of the reduced section was 2 mm and 1.5 mm respectively. The tensile test was performed using MTS Universal Testing Machine at room temperature. These tests were performed until fracture at 10^{-3} s^{-1} strain rate in triplicates for each alloy condition.

Micro-indentation was employed to characterise the mechanical properties such as elastic modulus and microhardness of the alloys. Indentation was carried out at room temperature using a CSM2-107 Tester equipped with a pyramidal Vickers indenter. The test operated as a load-controlled system, involving indents arranged in a five-by-two pattern with a 500 μm spacing between them. A maximum load of 0.5 N was applied with a loading rate of 1 N/min. Each indent was held for a duration of 70 s.

2.5. Electrochemical measurements

Potentiodynamic polarization measurements were performed using a three-electrode cell. The experimental setup consisted of an electrochemical potentiostat (OrigaLys), Saturated Calomel electrode (SCE) as reference electrode, Platinum electrode as an auxiliary electrode, and the specimen as the working electrode. Simulated Body Fluid (SBF) was used as the electrolyte and the exposed area of the working electrode in SBF was 49 mm^2. Open Circuit Potential (OCP) was measured for 1800 s in SBF to ensure the stability of the system. Potentiodynamic polarization test was carried out with a scan rate of 0.2 mV s^{-1}, with constant stirring at 4 rpm and scan range of 1 V with respect to OCP. Statistical significance was assessed by examining three samples for each condition. Corrosion rate (CR, mmpy) was calculated using the following equation [29]:

$$CR\ (mmpy) = \frac{3.27 \times 10^{-3} \times I_{corr} \times E_w}{\rho} \quad (1)$$

where, E_w represents the equivalent weight of the material and ρ is the density of the material in g cm^{-3}.

2.6. Immersion test

Triplicate experimental samples of 7 × 7 × 2 mm^3 dimensions of each alloy condition were immersed in SBF solution at 37 °C within an incubator shaker set at 150 rpm for 21 days. Fresh SBF solution was replenished every 3 days. The mass of each sample and pH measurements of the SBF solution were recorded every 2 days. Surface topography was examined using a stereomicroscope (Keyence) and scanning electron microscope (SEM) at the end of 21 days.

2.7. In vitro cell studies

2.7.1. Cell culture

Osteoblastic MC3T3-E1 cell line (Sigma-Aldrich) derived from mouse calvaria were cultured in α-modified eagle medium (α-MEM, Gibco) supplemented with 10 %(v/v) Fetal bovine serum (FBS, Dominique Dutscher) and 1 % (v/v) concentration of antibiotic Penicillin-Streptomycin. Cells were split at 80 % confluency and were passaged with Trypsin-EDTA (Dominique Dutscher). Passage 17–20 cells were used during the cell culture study.

RAW-Blue™ cells (InvivoGen) are designed to monitor inflammatory responses. They are derived from the murine RAW 264.7 macrophage cell line and feature a NF-κB/AP-1-inducible secreted embryonic alkaline phosphatase (SEAP) reporter gene. Exposition to inflammatory stimuli induces signalling pathways leading to the activation of NF-κB/AP-1 promoter of the reporter gene, and the subsequent production of SEAP. RAW-Blue™ cells were cultured in Dulbecco's Modified Eagle Medium (DMEM, Dominique Dutscher) supplemented with 10 % (v/v) heat-inactivated FBS and 200 μg/ml Zeocin (InvivoGen). Cells were passaged at 80 % confluency and were detached with cell scraper. Passage 6–9 cells were used during the cell culture.

All the cultures were maintained at 37 °C in a humidified atmosphere of 5 % CO_2.

2.7.2. Preparation of alloy extracts/conditioned medium

The cytocompatibility of the alloys with MC3T3-E1 cells was determined using an indirect method as described in ISO-10993-5 [30]. The samples were polished as mentioned above and sterilized with 100 % ethanol followed by UV sterilisation. After sterilization, samples were immersed immediately in α-MEM in the material surface to medium volume ratio of 1.25 cm^2/mL and kept in incubator shaker at 100 rpm at 37 °C. After 24 h, the conditioned medium (CM) was extracted and centrifuged at 3000 rpm for 15 min to remove the debris. The supernatant was then collected and called as α-MEM-CM.

2.7.3. Cytocompatibility assessment with MC3T3-E1 cells

Parallel to the onset of extraction, MC3T3-E1 cells were seeded at a density of 5000 cells per well in 96 well plate and pre-cultured for 24 h at 37 °C. After 24 h culture, the cell culture media was replaced with 100 % concentrated α-MEM-CM. Cells cultured in fresh DMEM medium is used as control. Cell viability was quantitatively determined for day1, 3 and 6 by MTS assay (Promega) according to the manufacturer' instruction. The 96-well plate was kept in the incubator for 3 h and after the incubation period, absorbance was recorded with the multi-mode microplate reader (CLARIOstar, BMG Labtech) at 490 nm. All the measurements were carried out in triplicates.

MC3T3-E1 cells cultured in indirect method for day1, 3 and 6 were imaged under confocal microscope (Zeiss LSM780) to study their cytoskeletal organization and cell morphology. Cells were seeded at a density of 2 × 10^4 cells per well of 24 well plate. Coverslips with cells cultured in fresh α-MEM were considered as control. On respective day points, cells were fixed with 4 % formaldehyde in PBS for 15 min and permeabilized with 0.1 % Triton X-100 for 15 min at room temperature. Cells were gently washed with PBS three times prior to each step. Blocking was done with 1 % Bovine Serum Albumin (BSA, Sigma) in PBS for 30 min.

No PBS wash was given after blocking step. Then, the cells were incubated in Phalloidin-iFluor 488 (Abcam ab176753, 1:2000 dilution) in 1 % BSA for 40 min in dark for F-actin staining. After three PBS washes, nuclei staining was done with Hoechst 33,258 (Santa Cruz, 1:2000 dilution) in PBS for 5 min in dark. Finally, the cells were washed with PBS and respective coverslips mounted on a glass slides using fluoromount aqueous mounting medium (Invitrogen). The stained cells were imaged in confocal microscope using 40× oil immersion objective. The images were processed using ZEISS Zen 3.9 software.

2.7.4. Inflammatory response

The conditioned medium of the alloys was prepared in DMEM cell medium using the above-mentioned procedure and called as DMEM-CM. To study the inflammatory response, DMEM-CM was diluted to 25 % and 50 % dilution using fresh DMEM, called as 0.25 DMEM-CM and 0.5 DMEM-CM, respectively.

RAW Blue^{TM} macrophages were seeded in 96 well plate with a seeding density of 7.2×10^4 cells per well in DMEM medium (10 % v/v heat-inactivated FBS, without any antibiotics). After 24 h of culture, the cell medium was replaced with 0.25DMEM-CM and 0.5DMEM-CM in the respective wells followed by a LPS (Escherichia coli 055B5; Sigma-Aldrich) stimulation for 24 h at 37 °C and 5 % CO_2. Two concentrations (0.1 ng/mL and 1 ng/mL) of LPS stimulation were given separately to the macrophages for 24 h. Cells cultured in DMEM medium were used as control. At the end of the LPS stimulation, 20 μL of cell supernatant was added to 180 μL of Quanti-Blue^{TM} solution and was incubated for 2 h at 37 °C. Quanti-Blue^{TM} solution contains chromogenic substrate for SEAP (Secreted Embryonic Alkaline Phosphate), which will help to measure the SEAP concentration in the cell supernatant. After 2 h incubation, the absorbance was recorded using microplate reader at 620 nm.

2.8. Statistical analysis

All the quantitative analyses were studied in triplicates for each sample/condition and each experiment was conducted at least three times. Data analysis and graphs were carried out using GraphPad Prism and Origin software. One-way ANOVA test was performed to determine the statistical significance of the results.

3. Results and discussion

3.1. Microstructure

Microstructural analysis of the as-cast Mg alloys was investigated through EDS analysis and they are tabulated in Table 2. The crystalline phases of the alloys were analysed using XRD technique. The X-Ray diffractograms shown in Fig. 1 were indexed using the standard ICDD database. All the Mg alloys exhibited the complete spectrum of α-Mg XRD reflections. There were no peaks corresponding to the binary Mg–Zn and Mg–Ca phases. The ternary phase of $Ca_2Mg_6Zn_3$ was indexed in all the alloy systems.

Table 2
Chemical compositions of as-cast Mg–Zn–Ca alloys.

Material	Elemental composition (wt%)			Zn/Ca atomic ratio
	Mg	Zn	Ca	
CZ00	100	–	–	–
CZ01	Balance	0.1 ± 0.01	0.2 ± 0.01	0.3
CZ02	Balance	0.2 ± 0.01	0.2 ± 0.02	0.6
CZ03	Balance	0.3 ± 0.01	0.2 ± 0.01	0.9
CZ04	Balance	0.4 ± 0.01	0.2 ± 0.01	1.2

Fig. 2 presents optical micrographs illustrating the as-cast Mg–*x*Zn-0.2 wt% Ca alloys, where *x* represents the Zn content ($x = 0.1$, 0.2, 0.3, and 0.4 wt%). Optical micrographs of the as-cast pure Mg (CZ00) are depicted in Fig. S1. The average grain size of these Mg–Zn–Ca alloys was determined using the linear intercept method, and the results are tabulated in Table 3. Analysis of the optical micrographs reveals that an increase in Zn content and Zn/Ca atomic ratio leads to a refinement in the grain size, reducing it from 115.6 μm to 41.96 μm.

The reduction of grain size can be ascribed to the growth-restricted factor (Q) [31], a parameter that quantifies the solute effect in alloy systems concerning both grain refinement and growth. The formula for Q is $Q = mC_o(k - 1)$, where m represents the gradient of the liquidus line of a binary alloy, C_o is the bulk concentration of the solute, and k is the equilibrium partition coefficient of the solute. A solute with a higher Q value is anticipated to demonstrate greater efficacy in refining grains due to its more pronounced constitutional undercooling effect [31]. Mg–Zn system exhibits a steeper slope of the liquidus line ($m = 6.04$ °C/wt%) in contrast to Mg–Ca ($m = 2.12$ °C/wt%), indicating a higher potential for Zn to induce grain size reduction. Consequently, the growth restriction factor (Q) increases when Zn is introduced into the MgCa alloy.

Scanning electron micrographs in Back Scattered Electron (BSE) mode of the alloys along with respective EDS maps are depicted in Fig. 3. This confirmed the presence of a uniformly distributed α-Mg phase, along with the precipitation of secondary phases in all alloys. The chemical composition of these secondary phases was analysed through EDS and presented in Fig. 4. From Fig. 3 and Table 3, it is evident that the volume fraction of secondary phases decreases from CZ01

Table 3
Average grain size values and secondary phase volume fraction of Mg-x Zn-0.2 wt% Ca ($x = 0.1$, 0.2, 0.3, and 0.4 wt%). ($n = 5$).

Material	Grain size (μm) Mean±S.D for $n = 5$	Secondary phase volume fraction (%)
CZ01	115.6 ± 6.7	0.96 ± 0.05
CZ02	91.2 ± 1.3	0.3 ± 0.01
CZ03	75.4 ± 4.7	0.1 ± 0.03
CZ04	42.0 ± 2.2	1.2 ± 0.01

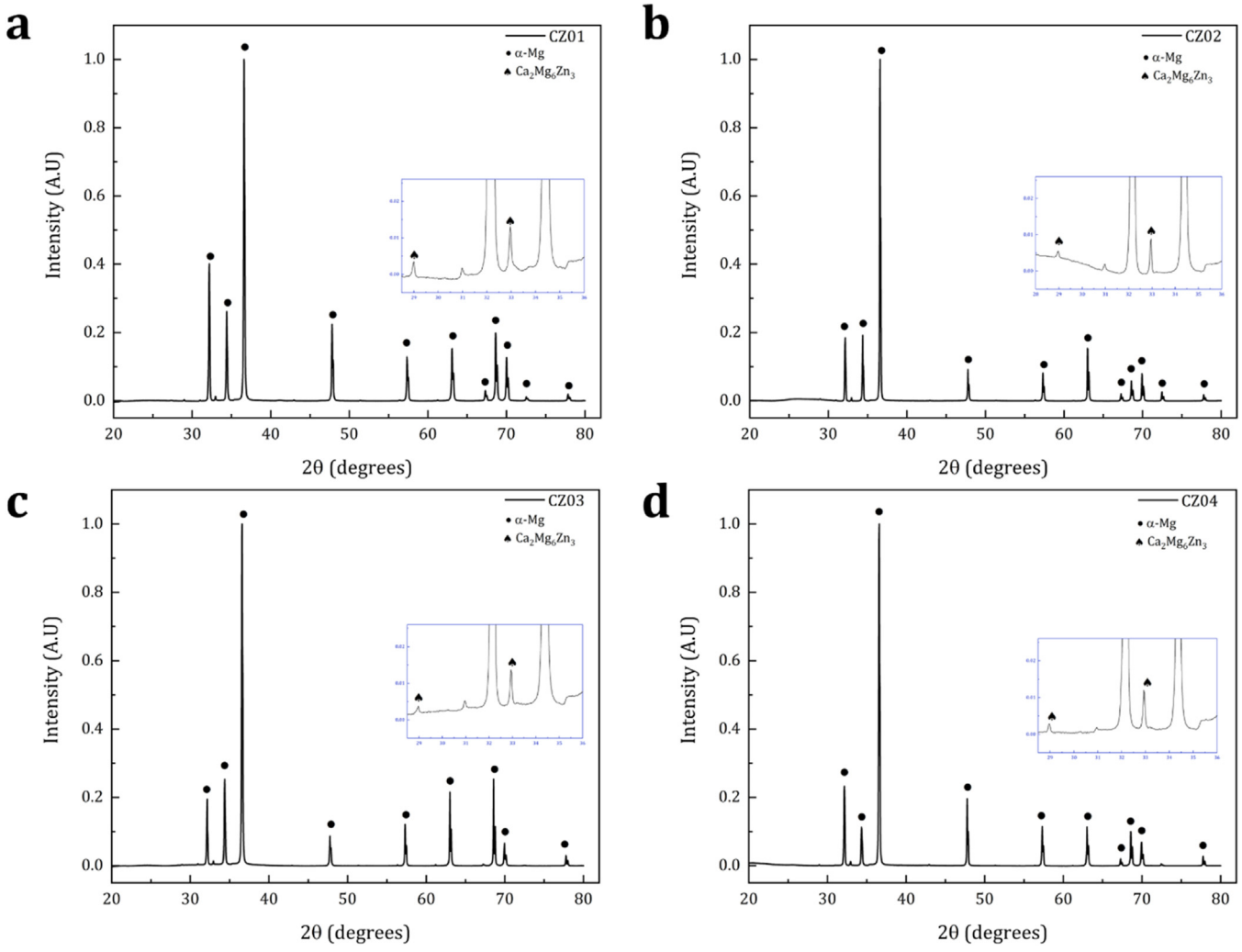

Fig. 1. X-Ray Diffraction patterns of (a) CZ01, (b) CZ02, (c) CZ03 and (d) CZ04.

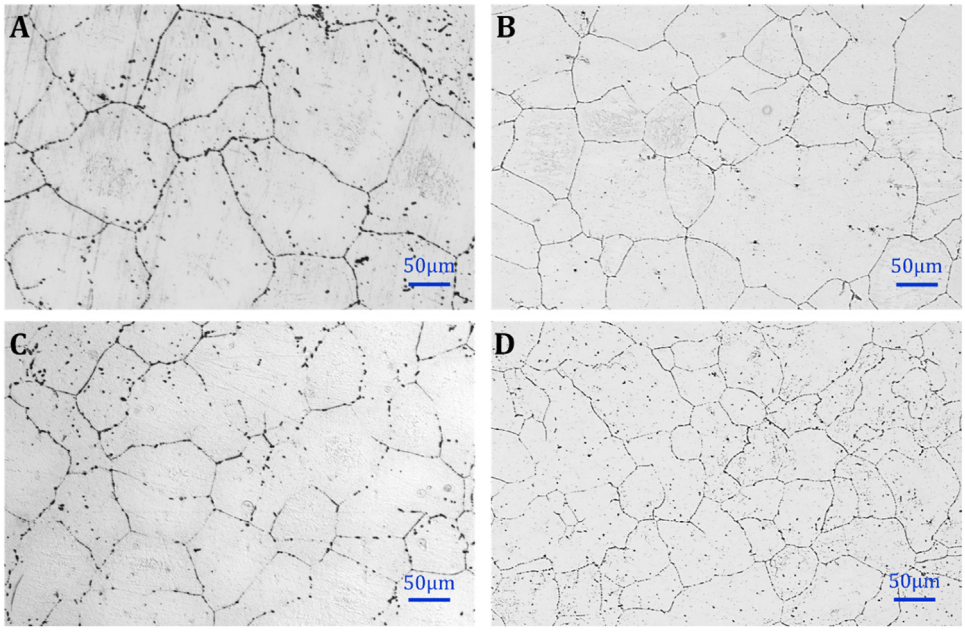

Fig. 2. Optical micrographs of (a) CZ01, (b) CZ02, (c) CZ03 and (d) CZ04.

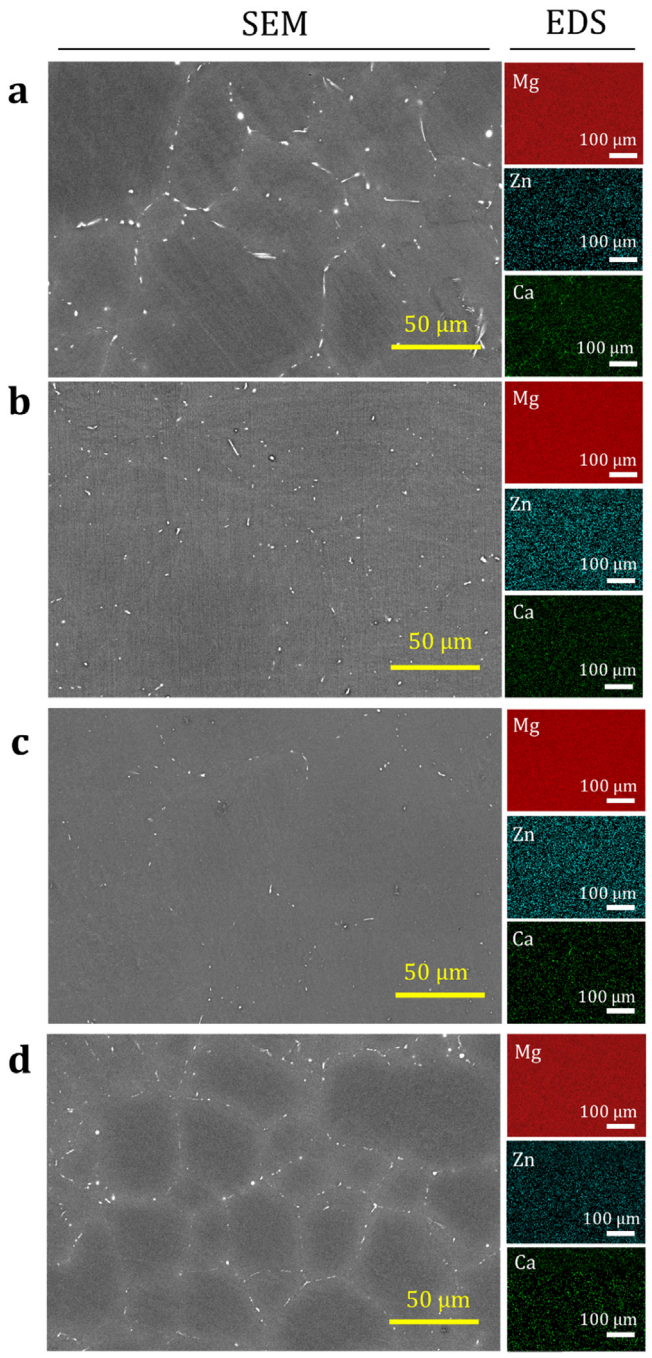

Fig. 3. SEM micrographs in BSE mode along with EDS mapping of (a) CZ01, (b) CZ02, (c) CZ03 and (d) CZ04.

to CZ03, then increases in CZ04. In terms of Zn/Ca atomic ratio, the alloy with a Zn/Ca atomic ratio of 0.9 exhibits the lowest volume fraction of secondary phases compared to the other investigated alloys. This could be due to difference in the atomic radius of Ca (0.18 nm), Mg (0.15 nm) and Zn (0.135 nm) [32]. The introduction of larger Ca atoms into the solid solution raises the Mg-lattice parameter, whereas the smaller Zn atoms have the opposite effect [33]. Previous studies suggest that Zn becomes part of the Mg_2Ca precipitates, which may then undergo a transformation into the ternary phase CaMgZn [33]. This transformation serves to decrease the lattice misfit between the precipitates and the Mg matrix. The enhanced lattice matching is expected to result in an increased rate of homogeneous nucleation, leading to a finer distribution of precipitates [34,35].

Furthermore, the observed trend in secondary phase volume fraction can be attributed to the effect of lattice misfit on the formation of these phases. Previous studies have demonstrated that a high lattice misfit can lower the nucleation energy barrier for precipitation, resulting in an increased formation of precipitates or secondary phases. The lower elemental segregation in CZ02 and CZ03 could be attributed to the influence of low lattice misfit leading to low solute accumulation at the grain boundaries and dislocation [36–38]. In this study, CZ04 exhibits the maximum volume fraction of secondary phases, indicating the highest lattice misfit among the alloys. Conversely, CZ03, which shows the minimum volume fraction of secondary phases, could attribute to the lowest lattice misfit.

XRD analysis confirms the presence of the $Ca_2Mg_6Zn_3$ ternary phase, aligning with findings from the EDS analysis. However, a slight mismatch is observed between the XRD spectrum peaks and the chemical composition of $Ca_2Mg_6Zn_3$ as indicated by the EDS analysis (Fig. 4). This mismatch could be attributed to variations in interplanar distances resulting from slight differences in Zn or Ca content. It was observed that higher Zn content led to lattice contraction, whereas increased Ca content resulted in lattice expansion, all while maintaining the suggested hexagonal structure [39].

3.2. Mechanical properties

Fig. 5 depicts the mechanical properties of as cast Mg (CZ00) and other Mg–*x*Zn–0.2Ca alloys, as revealed by the uniaxial tensile test. As compared to CZ00, it is evident from Fig. 5 (a and b) that micro-alloying with Zn and Ca has enhanced the mechanical properties of the Mg–*x*Zn–0.2Ca alloys, in terms of Elastic Modulus (E), Yield strength (YS) and Ultimate Tensile Strength (UTS). Using the Oliver and Pharr method [40], the elastic modulus ($E_{O/P}$) and micro-hardness of these alloys were calculated. Fig. 6a illustrates the load-displacement curves that closely align with the mean values of elastic modulus and micro-hardness of the alloys. Fig. 6b presents a graphical representation of the $E_{O/P}$ and micro-hardness of these alloys.

The elastic modulus (E) calculated from the tensile test, decreases in the order: CZ04>CZ01>CZ02>CZ03. Among all the studied alloys, CZ04 showed the maximum E value of 55.9 GPa while CZ03 shows the minimum E value of 36.8 GPa. CZ03 showed a value of E very close to the elastic modulus of natural bone (~20 GPa) [41]. The phase composition analysis of the Mg–*x*Zn–0.2Ca alloys in this study confirms the presence of the $Ca_2Mg_6Zn_3$ secondary phase, which precipitates along the grain boundaries and within the inner grains. As the Zn content increases from 0.1 wt% to 0.4 wt%, there is a noticeable rise in the micro-hardness of

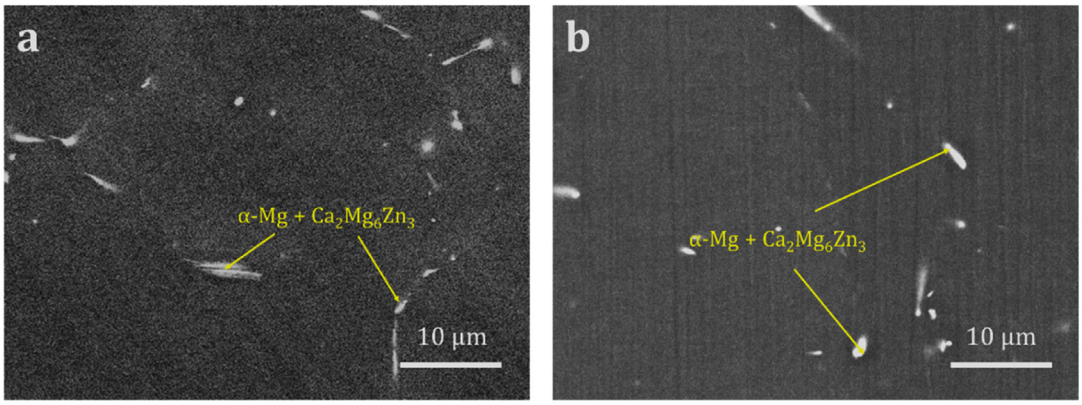

Secondary phase (CZ01)	Elemental composition (wt%)		
	Mg	Zn	Ca
α-Mg + $Ca_2Mg_6Zn_3$	75.4±0.2	17.3±0.2	7.4±0.1

Secondary phase (CZ02)	Elemental composition (wt%)		
	Mg	Zn	Ca
α-Mg + $Ca_2Mg_6Zn_3$	68.8±0.2	21.7±0.2	9.5±0.1

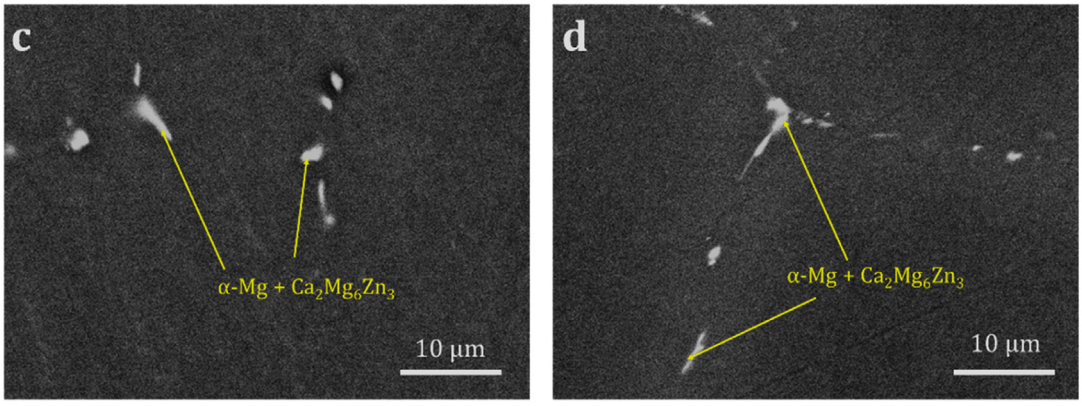

Secondary phase (CZ03)	Elemental composition (wt%)		
	Mg	Zn	Ca
α-Mg + $Ca_2Mg_6Zn_3$	65.3±0.2	24.4±0.2	10.3±0.1

Secondary phase (CZ04)	Elemental composition (wt%)		
	Mg	Zn	Ca
α-Mg + $Ca_2Mg_6Zn_3$	53.1±0.2	36.2±0.2	14.3±0.1

Fig. 4. EDS point analysis of the secondary phases of (a) CZ01, (b) CZ02, (c) CZ03 and (d) CZ04.

the alloys compared to pure Mg (CZ00). CZ04 exhibits the maximum micro-hardness of 57.5 HV and the highest $E_{O/P}$ of 39.4 GPa. Conversely, CZ03 shows the minimum $E_{O/P}$ of 33.7 GPa among all the alloys, with a micro-hardness of 53.5 HV. This indicates that the addition of Zn and Ca to the pure Mg matrix has improved both the elastic modulus and micro-hardness of the alloys.

The increasing trend in micro-hardness with higher Zn content is attributed to the presence of $Ca_2Mg_6Zn_3$ as a secondary phase, grain size reduction, and solid solution strengthening [15,42]. However, a synergistic effect of grain size and volume fraction of secondary phases plays a role in determining the mechanical properties of the Mg alloys [43]. In both tensile and micro-indentation test, CZ03 showed the minimum value for E and $E_{O/P}$. The precipitate strengthening effect significantly influences the elastic modulus of the as-cast Mg alloys [44,45]. In Fig. 3 and Table 3, CZ03, has the lowest volume fraction of the secondary phase, hence it could be the reason for exhibiting the lowest elastic modulus among all the as-cast alloys.

The UTS and ductility of the alloys increases with increasing Zn content and Zn/Ca atomic ratio. Previous literature studies have confirmed the enhancement of strength and ductility in as-cast Mg alloys through grain refinement [46]. In this study, CZ04 showed maximum UTS of 198.5 MPa and CZ01 showed the minimum UTS of 147.2 GPa, among all the Mg–*x*Zn–0.2Ca alloys. This reveals that addition of Zn and Ca affects the tensile properties. This could be attributed to the solid solution strengthening effect from the Zn and Ca alloying [47], resulting in higher tensile strength in alloys as compared to as-cast Mg (107.5 MPa).

The yield strength of the alloys increases in the order: CZ01<CZ02<CZ03<CZ04. This trend indicates the effect of grain refinement observed in the microstructure of alloys. In accordance to the Hall–Petch relationship, grain size reduction results in enhanced yield strength [48]. It has been reported that tension twining occurs when tensile stress is applied in HCP materials [49]. This stress twinning follows the Hall–Petch relationship. The initial yielding behavior of the Mg alloys is primarily influenced by the nucleation, propaga-

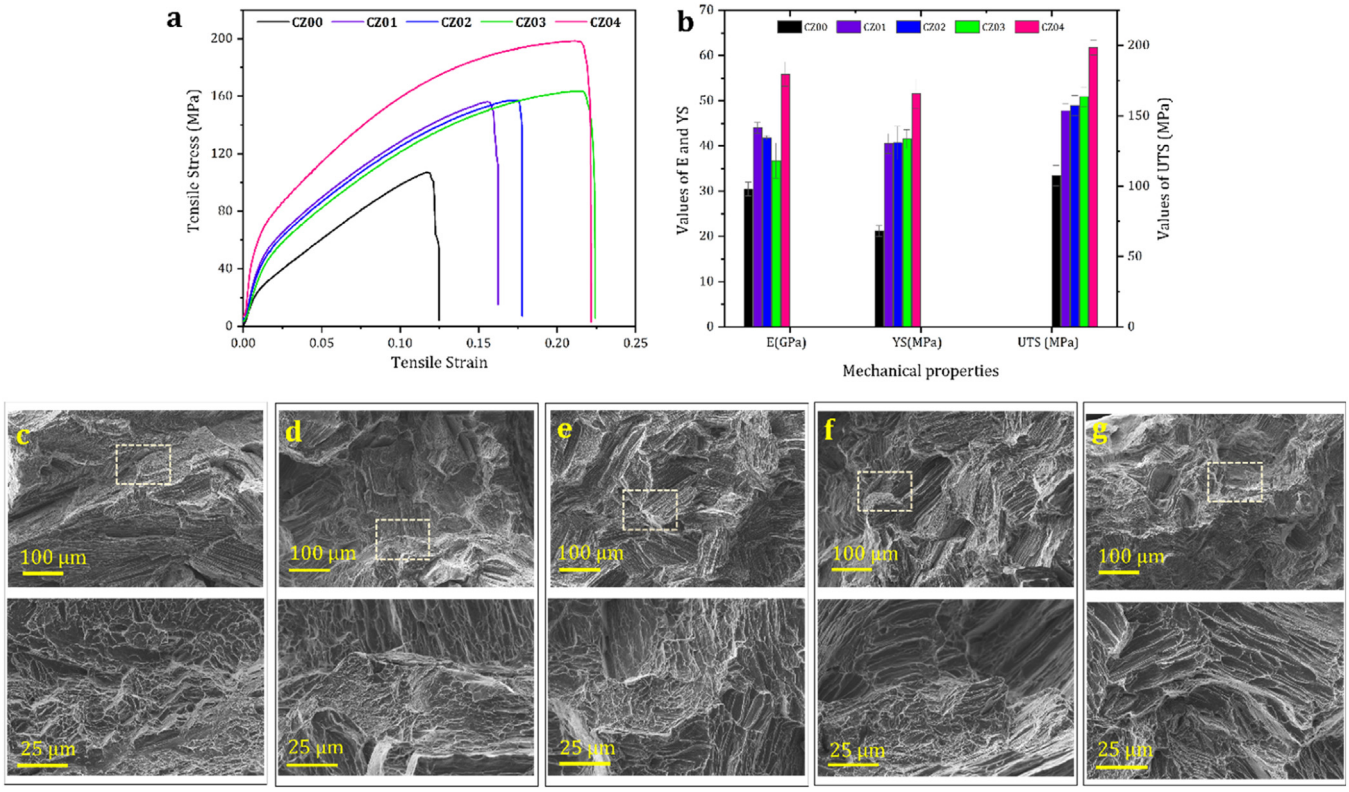

Fig. 5. Mechanical properties of Mg–*x*Zn–0.2 Ca alloys revealed by uniaxial tensile test: (a) Tensile stress vs tensile strain curves, (b) bar graph showing Elastic Modulus (E, GPa), Yield strength (YS, MPa) and UTS (GPa) as mean± S.D for $n = 3$, (c–g) fractographs of (c) CZ00, (d) CZ01, (e) CZ02, (f) CZ03 and (g) CZ04. Low magnification (Scale bar =100 µm) fractographs with dotted box indicates the area shown at higher magnification (Scale bar =25 µm.

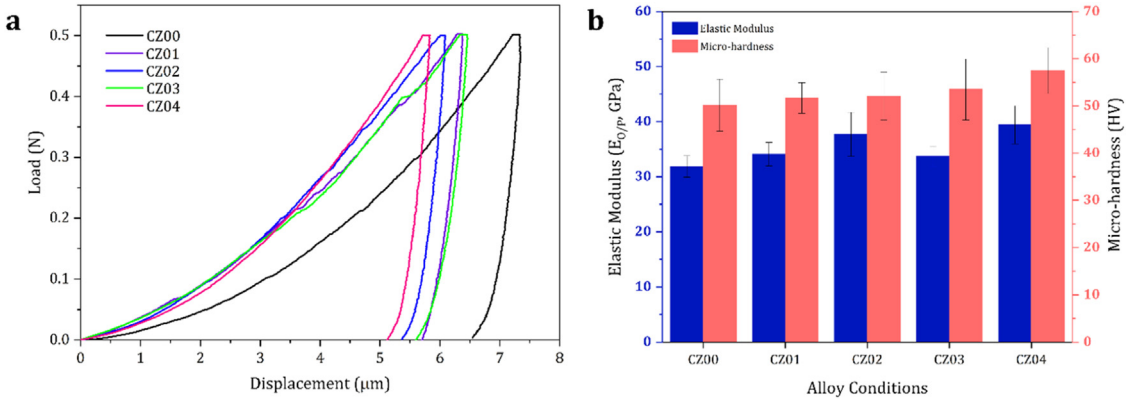

Fig. 6. Mechanical properties of Mg–*x*Zn–0.2 Ca alloys. (a) Load–displacement curves and (b) graphical representation of Elastic modulus ($E_{O/P}$, GPa) and micro-hardness (HV) of the alloys.

tion, and transfer of twins to neighbouring grains. Initially, a twin nucleates at a potential site, such as a grain boundary (GB), followed by rapid propagation and subsequent termination at an adjacent GB. When a twin terminates at a GB, it induces a localized stress concentration at the twin tip, which facilitates the nucleation of twinning in the adjacent grain [48,50]. The fractographs illustrated in Fig. 5 (c–g) shows elongated grooves called "flutes" which are believed to be induced by tensile twins, which further confirms the tensile twinning [51]. Presence of dimples in the fractographs across all systems confirms that the fracture mode is ductile [51,52].

3.3. Corrosion behaviour

Fig. 7 depicts the potentiodynamic polarization curves of pure Mg (CZ00) and all as-cast Mg alloys. The E_{corr} and I_{corr} values were determined through the Tafel extrapolation method and are presented in Table 4. The corrosion rates (mm yr^{-1}) for all samples were calculated using Eq. (1) and are summarized in Table 4.

The electrochemical parameters of CZ03 reveal that it demonstrates minimum I_{corr} value of 1.15×10^{-4} A cm^{-2} and an E_{corr} of −1.63 V, as compared to pure Mg and all

Table 4
Electrochemical parameters of as-cast Mg–*x*Zn–0.2Ca alloys ($n = 5$).

Material system	E_{corr} (V)	I_{corr} ($\times 10^{-4}$) (A cm^{-2})	Equivalent weight (E_w)(g)	CR (mm yr^{-1})
CZ00	−1.7 ± 0.02	2.86 ± 0.11	12.150	6.4 ± 0.03
CZ01	−1.69 ± 0.01	2.5 ± 0.09	12.167	5.6 ± 0.31
CZ02	−1.7 ± 0.05	1.5 ± 0.29	12.175	3.3 ± 0.25
CZ03	−1.63 ± 0.04	1.15 ± 0.05	12.183	2.5 ± 0.12
CZ04	−1.72 ± 0.01	1.58 ± 0.1	12.190	3.5 ± 0.3

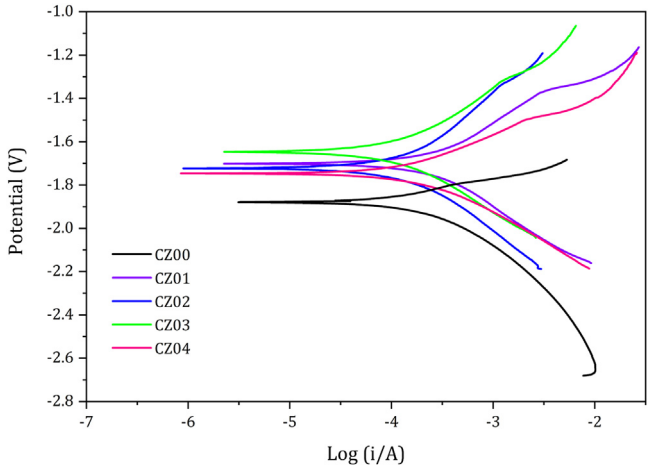

Fig. 7. Tafel plots obtained from Potentiodynamic polarisation measurement of as-cast pure magnesium (CZ00) and other Mg–*x*Zn–0.2Ca alloys.

other investigated alloys. This results in a calculated corrosion rate of 2.5 mm yr^{-1} for CZ03. While CZ01 shows the maximum Icorr value of 2.5 × 10^{-4} A cm^{-2}, compared to all other investigated alloys. The corrosion rate in the micro-alloyed as-cast Mg–*x*Zn–0.2Ca alloys increases in the order: CZ03<CZ02<CZ04<CZ01<CZ00. This indicates a direct influence of microstructure on the corrosion behaviour of the as-cast alloys. Previous reports on MgZnCa alloys have demonstrated that minimum corrosion rate could be achieved with a balanced volume fraction of secondary phases and grain size. The corrosion rate in as-cast alloys decreases with grain size refinement [53,54] and increases with increasing density of secondary phases, leading to further increase in the I_{corr} values. Additionally, secondary phases precipitates at the grain boundaries could result in severe galvanic corrosion attack in comparison to the precipitates at the interior of the grains [55]. This occurs due to the difference in the electrochemical potential of the precipitate and matrix. The standard electrode potential decreases in the order: $Ca_2Mg_6Zn_3$> α-Mg>Mg_2Ca [20]. From the grain size analysis shown in Table 3, it was observed that CZ01 has the larger grain size among all the other as-cast alloys and the grain size decreases in the order: CZ01>CZ02>CA03>CZ04. Fig. 3 depicts the volume fraction of secondary phases presents in the studied alloys and decreases in the order: CZ01>CZ04>CZ02>CZ03. Lu. Y., et al. [56] have reported that in as-cast MgZnCa alloys, the volume fraction of secondary phases was dominant over the beneficial effect of fine grain size. Similar observations are realised as in the case of CZ03 alloy presenting better corrosion properties among all the studied alloys.

3.4. Degradation studies

Fig. 8 summarizes the results of the degradation studies of the Mg alloys in SBF for 21days. The weight loss (%) of each Mg alloys is illustrated graphically in Figs. 7a and 8b show the pH change observed over 21 days in Mg alloys. At the end of 21 days of degradation, the corroded surfaces were observed under optical and electron microscope. Fig. 8-(c–f) depicts the SEM micrographs of the corroded surface of CZ01, CZ02, CZ03, and CZ04 respectively, along with the corresponding EDS analysis spectrums.

The degradation of Mg alloys in SBF undergoes the following chemical reaction [57]:

$$Mg \rightarrow Mg^{2+} + 2e^{-} \text{ (anodic)} \quad (2)$$

$$2H_2O + 2e^{-} \rightarrow H_2 + 2OH^{-} \text{ (cathodic)} \quad (3)$$

$$Mg^{2+} + 2OH^{-} \rightarrow Mg(OH)_2 \quad (4)$$

Cl^{-} ions present in SBF react with $Mg(OH)_2$ to produce $MgCl_2$, releasing additional OH^{-}ions as byproducts [58]. This reaction leads to a rapid increase in pH, as depicted in Fig. 8b. Among the magnesium alloys, pure Mg (CZ00) exhibits the highest pH change of 10, while CZ03 shows the lowest change at 8.5 compared to the other alloys. Fig. 8a illustrates the maximum degradation for CZ00, and the degradation rate follows the order of CZ01 > CZ04 > CZ02 > CZ03 in terms of weight loss (%). This degradation pattern aligns with the electrochemical corrosion rate presented in Table 4.

A noticeable weight increase is observed in pure Mg and other alloys on day 3, which could be attributed to the strong adhesion of corrosion products to the material surface. However, as degradation progresses, the corrosion products detach, resulting in a decreasing trend in weight change (Fig. 8a). Consequently, phosphate ions (PO_4^{3-}) and Ca^{2+} ions in SBF likely react with OH^{-} ions to form hydroxyapatite (HA, $Ca_{10}(PO_4)_6(OH)_2$), as observed in the EDS analysis (Fig. 8-c–f) of the respective Mg alloys. Mg^{2+} serves as a crucial ionic substitution in biological apatite [59], leading to the formation of a corrosion product layer containing $Mg(OH)_2$, HA,

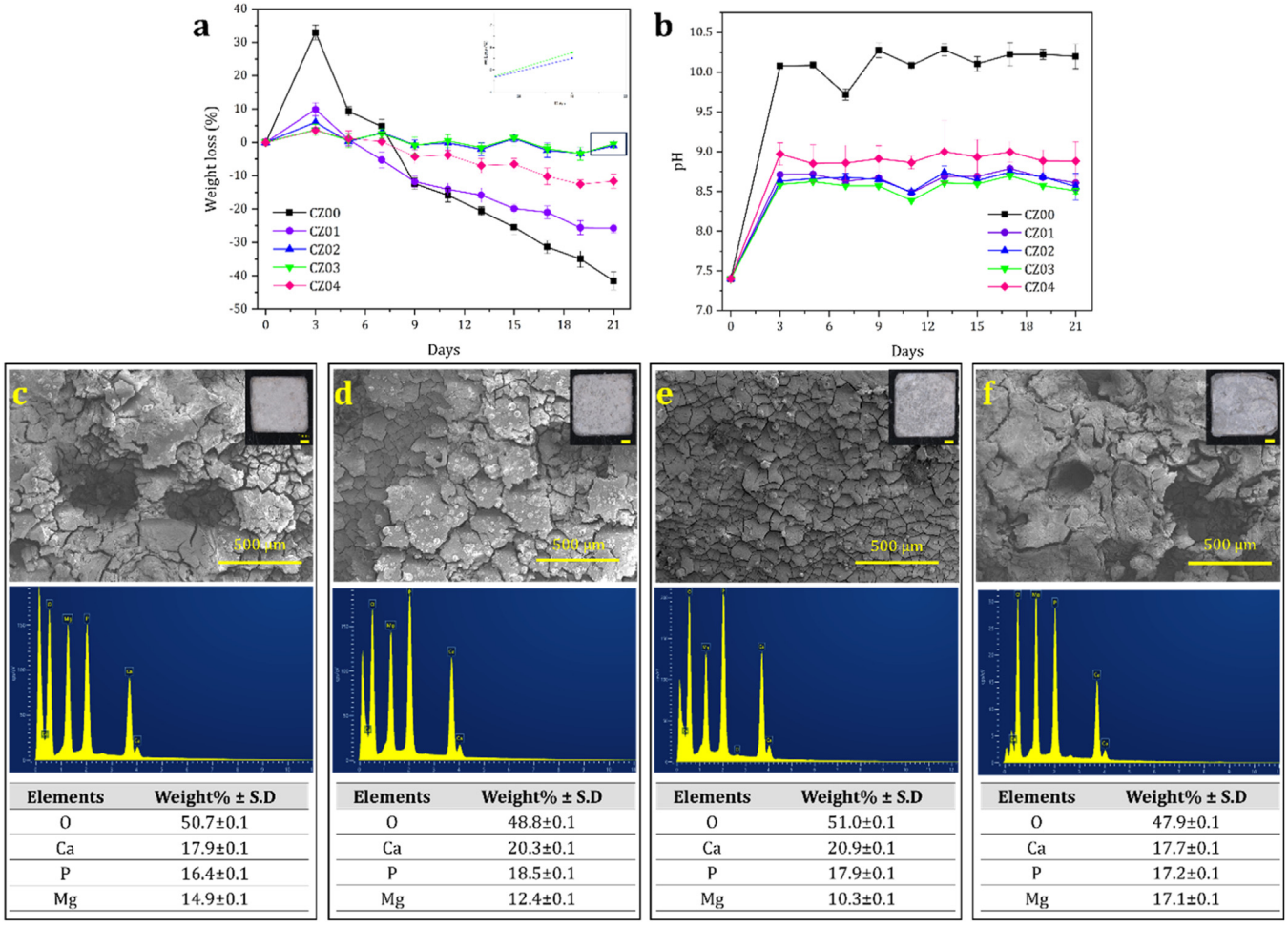

Fig. 8. Degradation behaviour of Mg–*x*Zn–0.2Ca alloys in SBF for 21days: (a) weight loss (%), (b) evolution of pH change of SBF. SEM micrographs showing surface morphology and EDS area analysis of 21 days degraded alloys (c) CZ01, (d) CZ02, (e) CZ03 and (f) CZ04. The insets in the SEM images are the optical images (Scale bar= 1 mm) of the corresponding alloys after 21 days of degradation in SBF.

and other Mg apatites that covers the surface (Fig. 8-c–f), subsequently decreasing the corrosion rate.

An early rise in pH values for the alloys was attributed to the accumulation of OH ions in the form of $Mg(OH)_2$ on their surfaces. As the immersion time increased to 3days, the pH value of alloys gradually rose to around 9.0, indicating a steady trend. This behavior is due to the formation of passive layer of $Mg(OH)_2$ and the subsequent precipitation of calcium phosphate as a top layer on the $Mg(OH)_2$ [60]. Concurrently, the consumption of calcium phosphate from the SBF led to an increase in the amount of hydroxyapatite precipitation on the surface. While the passive layer remains intact, the weight loss rate remains relatively stable, as indicated by a plateau on the weight loss (%) graph in Fig. 8(a). However, upon local destruction of the corrosion product film, localized corrosion initiates [61,62]. This leads to an increase in the corrosion rate, reflected by a downward trend in weight loss profile in Mg–*x*Zn–0.2Ca alloys.

Unlike CZ01 and CZ04, the corroded surfaces of CZ02 and CZ03 lack corrosion pits, possibly explaining their reduced degradation behaviour over 21 days. The presence of chloride

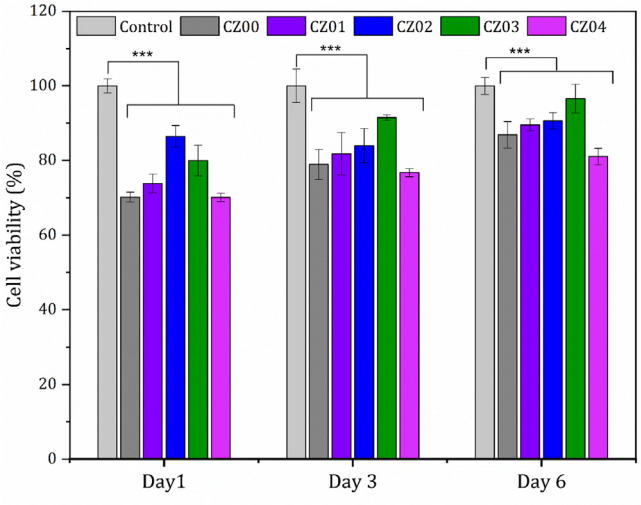

Fig. 9. Cell viability (%) measured by MTS assay absorbance at 490 nm for MC3T3-E1 cells cultured in conditioned medium (α-MEM-CM) with Mg alloys. Data represented are mean ± *S*.D for $n = 3$. One-way ANNOVA test was used to calculate the p values, where ***indicates $p < 0.001$.

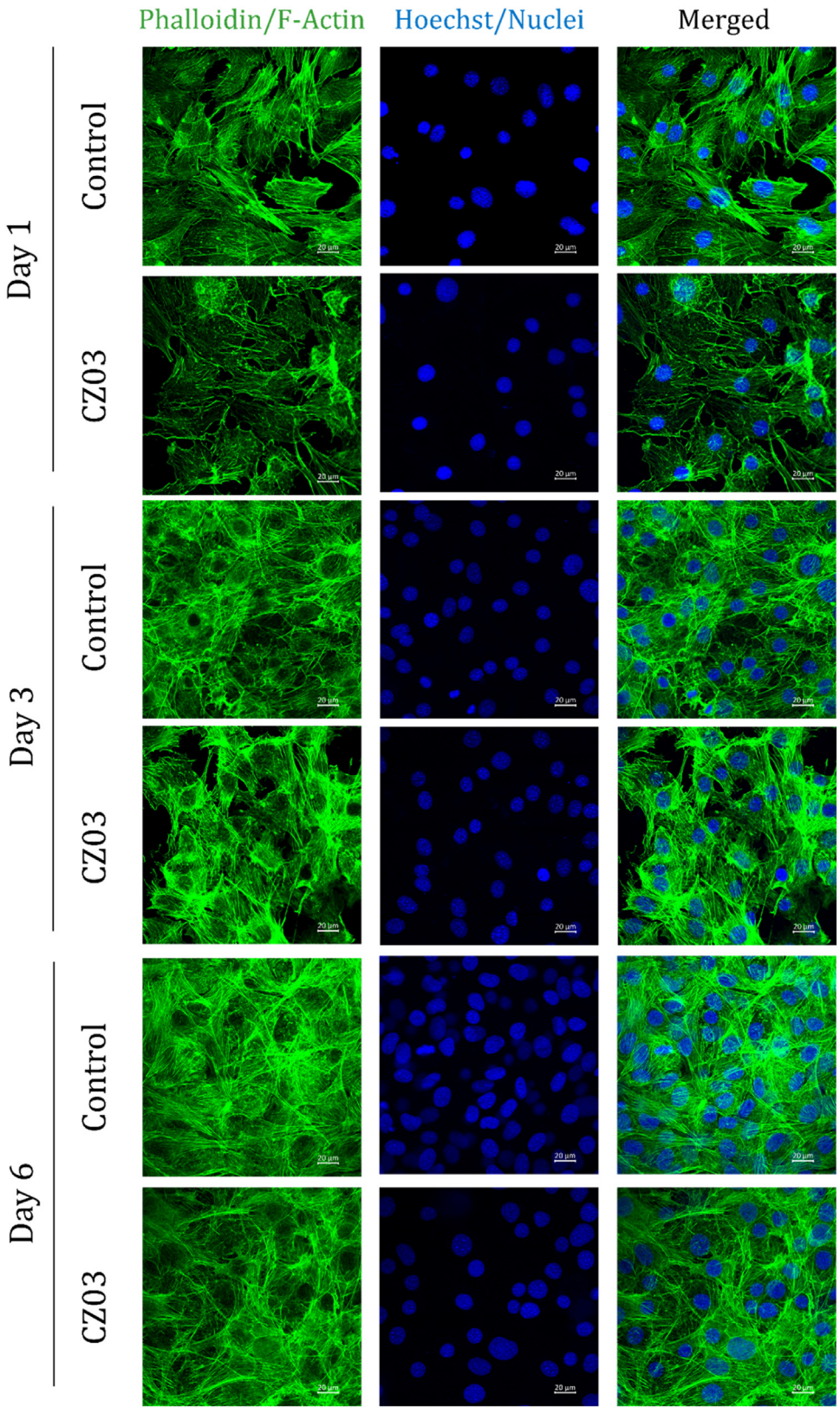

Fig. 10. Confocal micrographs of MC3T3-E1 cells cultured in conditioned medium (α-MEM-CM) with CZ03. F-actin fibers are stained with Phalloidin (green) and Nuclei with Hoechst (blue) with a scale bar of 20 µm.

ions influences the formation of hydroxyapatite (HA), causing HA to adopt a platy shape in the presence of chloride ions and a needle-like shape in their absence, while the composition of HA remains unaffected by Cl^-. This suggests that the degradation of the magnesium alloy enhances the precipitation of HA [63]. Previous studies have demonstrated that HA formation promotes osteoinductive and osteoconductive properties, contributing to the biocompatibility of Mg alloys [64].

3.5. In vitro cell studies

3.5.1. Cytocompatibility assessment with MC3T3 E1 cells

The cytocompatibility assessment utilized the conditioned medium prepared with various Mg alloys and Pure Mg. Fig. 9 illustrates the cell viability of MC3T3-E1 cells over a 6-day duration in the conditioned medium of all four alloys. In the initial 24 h of culture, all alloys displayed cell viability of ≥70 % compared to the Control, indicating the absence of cytotoxicity in the tested Mg alloys, in accordance with ISO-10993-5. Day 1 cell viability results revealed the impact of pH change and ion concentration in the conditioned medium on cell proliferation. The release of Mg^{2+} ions led to alkalinization of the cell medium, resulting in low metabolic activity on Day 1. However, by Day 3, an increase in cell viability was observed, suggesting that cells in the conditioned medium adapted to the environment and exhibited proliferation capability similar to the control [65]. The cell viability findings align well with the corrosion and degradation behaviour depicted in Figs. 7 and 8. CZ03 consistently demonstrates the highest cell viability over the 6-day cell culture period. This can be attributed to its lower corrosion rate and minimal release of metal ions, contributing to the maintenance of favourable pH conditions conducive to cell growth and proliferation. In addition to its desirable mechanical properties, corrosion resistance, and degradation rate, CZ03 exhibits superior cytocompatibility compared to the other investigated Mg alloys. This led us to conclude that CZ03 is the most promising alloy composition, both in terms of material and biological aspects. Consequently, CZ03 underwent further assessment to study its cytoskeletal arrangement and morphology through an indirect method utilizing confocal microscopy.

Fig. 10 presents representative confocal micrographs depicting MC3T3-E1 cells cultured in the conditioned medium of CZ03 for days 1, 3, and 6, with cells cultured in fresh αMEM medium serving as the Control. Cytoskeletal reorganization and alterations in cell proliferation indicate cell adhesion, proliferation, and functionality through the activation of cellular signalling pathways [66,67]. On day 1, cell proliferation for CZ03 was lower, with a non-uniform distribution of actin fibers compared to the control. However, by the beginning of day 3, there was an increase in cell proliferation for CZ03, evident from the rise in Hoechst-stained nucleus count. Additionally, a confluent layer of MC3T3-E1 cells similar to the control was observed on day 6. The confocal micrographs in Fig. 10 further validate the quantitative cell viability (%) presented in Fig. 9.

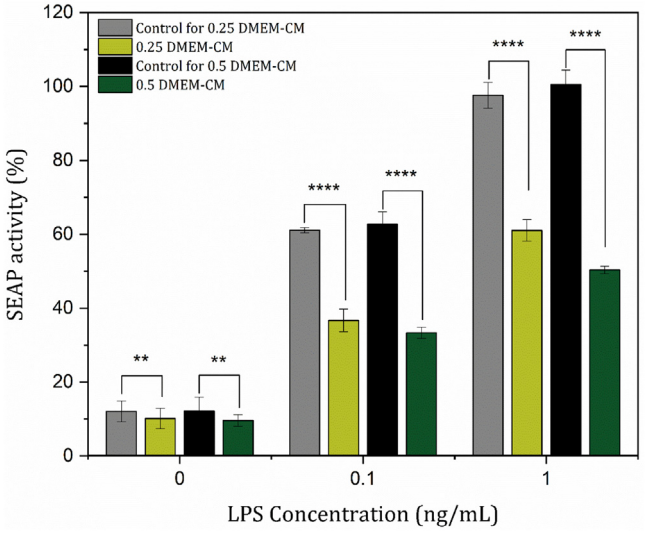

Fig. 11. Comparison of SEAP activity of RAW-Blue ™ cells to DMEM-CM extract of CZ03 at 25% (0.25 DMEM-CM) and 50 % dilution (0.5 DMEM-CM), with and without LPS stimulation. Data represented are mean ± *S*.D for $n = 3$. One-way ANNOVA test was used to calculate the p values, where ** indicates $p < 0.01$, ****indicates $p < 0.0001$.

3.5.2. SEAP activity

The study employed the conditioned medium of CZ03 at 25 % and 50 % extracts to investigate the inflammatory response in RAW-Blue macrophage cells. Fresh DMEM cell culture medium underwent incubation under the same conditions as the conditioned medium preparation for 24 h, referred to as S-DMEM. The control for the 25 % extract of CZ03 was created by combining fresh DMEM and S-SMEM in a 3:1 ratio. Likewise, the control for the 50 % extract of CZ03 was prepared by mixing fresh DMEM and S-DMEM in a 1:1 ratio.

Lipopolysaccharide (LPS) is a Toll-like Receptor 4 (TLR4) agonist which can induce potent inflammatory responses like TNF-α and IL-6 production via activating NF-κB signalling pathway [68]. In our model, production and activity of SEAP mimic cytokine production. Thus, LPS stimulation can be detected and quantified in terms of SEAP production. Fig. 11 shows the graphical representation of SEAP activity in absence/presence of LPS stimulation. It was observed that in absence of LPS, CZ03 alloy extracts do not express any pro-inflammatory response in RAW-Blue cells. While, in presence of LPS, CZ03 alloy extract exhibits downregulation of SEAP expression, in comparison to their respective Control conditions. An increase in the concentration of Mg alloys resulted in more decrease in the SEAP activity. Mg causes decrease in LPS/TLR4 binding extracellularly and results in decrease in cytokine production [69]. Another possible explanation for this downregulation of SEAP production could be the inhibition of NF-κB signalling pathway by Mg^{2+} ions [69–71]. Several studies reveal the impact of magnesium on decreasing the cytokine production by increasing IκBα levels, which is the basal inhibitor of NF-κB activation. Therefore, it can be inferred that Mg^{2+} ions in CZ03 alloy extract produced an

anti-inflammatory environment either by reducing LPS/TLR4 binding or via downregulating TLR- NF-κB signally pathway for SEAP production in RAW-Blue macrophage cells.

4. Conclusion

This study investigated the effects of micro-alloying Mg alloys with Zn and Ca, focusing on the mechanical, corrosion, and biocompatibility properties of these alloys for potential biomedical applications. The following key findings were observed:

- Micro-alloying of Mg alloys with Zn and Ca exhibited very fine particle size of Ca2Mg6Zn3 secondary phases.
- Among all the studied alloys, CZ03 with 0.3 wt% Zn and 0.2 wt% Ca (with Zn/Ca atomic ratio of 0.9), demonstrated the elastic modulus of 36.8 GPa which is close to natural bone, minimum corrosion rate, less degradation, and less pH change of SBF in 21 days immersion.
- All the alloys showed cytocompatibility $\geq$ 70 % towards MC3T3-E1 cells. During the cell viability assessment, CZ03 resulted to have the highest cell viability among all the alloys.
- Further investigation into the inflammatory response of CZ03 revealed a decrease in SEAP activity with an increase in CZ03 extract concentration.
- Based on these findings, it can be concluded that the as-cast Mg–0.3Zn–0.2Ca alloy is well-suited for biomedical bone fixation applications.
- Mg–0.3Zn–0.2Ca (CZ03) offers enhanced corrosion resistance, cytocompatibility, and anti-inflammatory properties. The novel MgZnCa alloy holds promise in reducing complications associated with post-secondary operations in biomedical applications

Data availability

All the data used in this paper and supplementary information are available upon reasonable request from the corresponding author.

CRediT authorship contribution statement

Manisha Behera: Writing – original draft, Methodology, Investigation, Data curation, Conceptualization. **Agnès Denys:** Methodology, Investigation, Formal analysis. **Rajashekhara Shabadi:** Writing – review & editing, Visualization, Supervision, Resources, Project administration, Methodology, Investigation, Funding acquisition, Formal analysis, Data curation, Conceptualization. **Fabrice Allain:** Writing – review & editing, Resources, Formal analysis, Data curation. **Cosmin Gruescu:** Resources.

Acknowledgement

The authors would like to acknowledge Dr. Marie-Ange Krzewinski, from UGSF lab, University of Lille for her help in confocal microscopy. This work was funded by European Union's Horizon 2020 Research and Innovation program and 'Magnesium based Nano Composites for Orthopedic Applications' MAGNACOM, project under the aegis of Programme for Early-Stage Researchers (PEARL, I-Site ULNE under the Marie Sklodowska-Curie grant agreement). This work was supported by University of Lille (France) and Hauts-de-France region.

Declaration of competing interest

The authors declare no competing interests.

Supplementary materials

Supplementary material associated with this article can be found, in the online version, at doi:10.1016/j.jma.2024.07.001.

References

[1] Y. Xin, T. Hu, P.K. Chu, Acta Biomater. 7 (2011) 1452–1459.
[2] J. Walker, S. Shadanbaz, T.B.F. Woodfield, M.P. Staiger, G.J. Dias, J. Biomed. Mater. Res. B Appl. Biomater. 102 (2014) 1316–1331.
[3] N. Hadrup, J.B. Sørli, A.K. Sharma, Toxicology (2022) 467.
[4] R.V. Badhe, O. Akinfosile, D. Bijukumar, M. Barba, M.T. Mathew, Toxicol. Lett. 350 (2021) 213–224.
[5] M.R. Rahimzadeh, M.R. Rahimzadeh, S. Kazemi, R.J. Amiri, M. Pirzadeh, A.A. Moghadamnia, Emerg. Med. Int. 2022 (2022) 1480553.
[6] A. Ivkovic, T.A. Stern, Psychosomatics 55 (2014) 296–302.
[7] L. Leyssens, B. Vinck, C. Van Der Straeten, F. Wuyts, L. Maes, Toxicology 387 (2017) 43–56.
[8] L.H. Campos Becerra, M.A.L. Hernández Rodríguez, H. Esquivel Solís, R. Lesso Arroyo, A. Torres Castro, Biomed. Phys. Eng. Express. 6 (2020).
[9] Z. Li, X. Gu, S. Lou, Y. Zheng, Biomaterials 29 (2008) 1329–1344.
[10] S. Zhang, X. Zhang, C. Zhao, J. Li, Y. Song, C. Xie, H. Tao, Y. Zhang, Y. He, Y. Jiang, Y. Bian, Acta Biomater. 6 (2010) 626–640.
[11] Y. Sun, B. Zhang, Y. Wang, L. Geng, X. Jiao, Mater. Des. 34 (2012) 58–64.
[12] F. Rosalbino, S. De Negri, A. Saccone, E. Angelini, S. Delfino, J. Mater. Sci. Mater. Med. 21 (2010) 1091–1098.
[13] H. Ibrahim, S.N. Esfahani, B. Poorganji, D. Dean, M. Elahinia, Mater. Sci. Eng. C 70 (2017) 870–888.
[14] Y. Jang, Z. Tan, C. Jurey, Z. Xu, Z. Dong, B. Collins, Y. Yun, J. Sankar, Mater. Sci. Eng. C 48 (2015) 28–40.
[15] N. Pulido-González, B. Torres, S. García-Rodríguez, P. Rodrigo, V. Bonache, P. Hidalgo-Manrique, M. Mohedano and J. Rams, *J. Alloys Compd.*, DOI:10.1016/j.jallcom.2020.154735.
[16] J. Geng, J.F. Nie, Mater. Sci. Eng.: A 653 (2016) 27–34.
[17] Y. Zhang, H. Jiang, Y. Wang, Z. Xu, Metals. (Basel) 10 (2020) 1–24.
[18] E. Mostaed, M. Sikora-Jasinska, L. Wang, A. Mostaed, I.M. Reaney, J.W. Drelich, JOM 72 (2020) 1880–1891.
[19] Y. Wang, H. Wang, X. Luo, G. Ren, W. Cheng, H. Hou, Int. J. Electrochem. Sci. 17 (2022), doi:10.20964/2022.08.39.
[20] H. xiang Li, S. kai Qin, Y. zhong Ma, J. Wang, Y. jin Liu, J. shan Zhang, Int. J. Miner., Metall. Mater. 25 (2018) 800–809.
[21] B. Zhang, Y. Wang, L. Geng, C. Lu, Mater. Sci. Eng.: A 539 (2012) 56–60.

[22] T. Homma, C.L. Mendis, K. Hono, S. Kamado, Mater. Sci. Eng.: A 527 (2010) 2356–2362.
[23] L.B. Tong, M.Y. Zheng, S.W. Xu, S. Kamado, Y.Z. Du, X.S. Hu, K. Wu, W.M. Gan, H.G. Brokmeier, G.J. Wang, X.Y. Lv, Mater. Sci. Eng.: A 528 (2011) 3741–3747.
[24] T. Homma, J. Hinata, S. Kamado, Philos. Mag. 92 (2012) 1569–1582.
[25] M.D. Costantino, A. Schuster, H. Helmholz, A. Meyer-Rachner, R. Willumeit-Römer, B.J.C. Luthringer-Feyerabend, Acta Biomater. 101 (2020) 598–608.
[26] C.J. Kirkpatrick, V. Krump-Konvalinkova, R.E. Unger, F. Bittinger, M. Otto, K. Peters, Biomol. Eng. 19 (2002) 211–217.
[27] S. Franz, S. Rammelt, D. Scharnweber, J.C. Simon, Biomaterials 32 (2011) 6692–6709.
[28] J.M. Anderson, A. Rodriguez, D.T. Chang, Semin. Immunol. 20 (2008) 86–100.
[29] G. Astm, in: Annual Book of ASTM Standards, 3, American Society for Testing and Materials (ASTM), 2009, pp. 237–239.
[30] R.F. Wallin, E.F. Arscott, Med. Dev. Diagn. Ind. 20 (1998) 96–98.
[31] Y. Jin, C. Blawert, H. Yang, B. Wiese, F. Feyerabend, J. Bohlen, D. Mei, M. Deng, M.S. Campos, N. Scharnagl, K. Strecker, J. Bode, C. Vogt and R. Willumeit-Römer, *Mater. Des.*, DOI:10.1016/j.matdes.2020.108980.
[32] J.C. Slater, J. Chem. Phys. 41 (1964) 3199–3204.
[33] E. Hehmann, E. Sommer, B. Predel, Mater. Sci. Eng. A. 125 (1990) 249–265.
[34] J.F. Nie, B.C. Muddle, Scr. Mater. 37 (1997) 1475–1481.
[35] R.E. Schäublin, M. Becker, M. Cihova, S.S.A. Gerstl, D. Deiana, C. Hébert, S. Pogatscher, P.J. Uggowitzer, J.F. Löffler, Acta Mater. 239 (2022) 118223.
[36] H. Mao, C. Zeng, Z. Zhang, X. Shuai, S. Tang, Materials 16 (2023) 6307.
[37] C. Schwalbe, A. Jacques, E. Galindo-Nava, C.N. Jones, C.M.F. Rae, J. Cormier, Mater. Sci. Eng.: A 740–741 (2019) 182–186.
[38] J.D. Robson, M.R. Barnett, Adv. Eng. Mater. 21 (2019) 1800460.
[39] T.V. Larionova, W.-W. Park, B.-S. You, Scr. Mater. 45 (2001) 7–12.
[40] W.C. Oliver, G.M. Pharr, J. Mater. Sci. Res. 7 (1992) 1564–1583.
[41] K.D. Hunt, V.D. O'Loughlin, D.W. Fitting, L. Adler, Med. Biol. Eng. Comput. 36 (1998) 51–56.
[42] L. Wei, J. Li, Y. Zhang and H. Lai, *Mater. Chem. Phys.*, 10.1016/j.matchemphys.2019.122441.
[43] F. Zhang, A. Ma, D. Song, J. Jiang, F. Lu, L. Zhang, D. Yang, J. Chen, J. Rare Earths 33 (2015) 93–101.
[44] L. Geng, B.P. Zhang, A.B. Li, C.C. Dong, Mater. Lett. 63 (2009) 557–559.
[45] H. Shi, C. Xu, X. Hu, W. Gan, K. Wu, X. Wang, J. Magn. Alloys 10 (2022) 2009–2024.
[46] Z. Zareian, M. Emamy, M. Malekan, H. Mirzadeh, W.J. Kim, A. Bahmani, Mater. Sci. Eng.: A 774 (2020) 138929.
[47] C. Li, H. Sun, X. Li, J. Zhang, W. Fang, Z. Tan, J. Alloys Compd. 652 (2015) 122–131.
[48] H. Yu, Y. Xin, M. Wang, Q. Liu, J. Mater. Sci. Technol. 34 (2018) 248–256.
[49] B.-C. Suh, J.H. Kim, J.H. Hwang, M.-S. Shim, N.J. Kim, Sci. Rep. 6 (2016) 22364.
[50] M.R. Barnett, M.D. Nave, A. Ghaderi, Acta Mater. 60 (2012) 1433–1443.
[51] S. Ravindran, G. Shankar, S. Suwas, R. Narasimhan, Acta Mater. 202 (2021) 350–365.
[52] E. Merson, V. Poluyanov, P. Myagkikh, D. Merson, A. Vinogradov, Mater. Sci. Eng.: A 772 (2020) 138744.
[53] Y. Zhang, X. Feng, Q. Huang, Y. Li, Y. Yang, J. Magn. Alloys 11 (2023) 1709–1720.
[54] K.D. Ralston, N. Birbilis, C.H.J. Davies, Scr. Mater. 63 (2010) 1201–1204.
[55] D. Orlov, K.D. Ralston, N. Birbilis, Y. Estrin, Acta Mater. 59 (2011) 6176–6186.
[56] Y. Lu, A.R. Bradshaw, Y.L. Chiu, I.P. Jones, Mater. Sci. Eng. C 48 (2015) 480–486.
[57] G. Song, D. Stjohn, J. Nairn, Y. Lit, Corros. Sci. 39 (1997) 855–875.
[58] Y. Wang, M. Wei, J. Gao, J. Hu, Y. Zhang, Mater. Lett. 62 (2008) 2181–2184.
[59] H. Kuwahara, Y. Al-Abdullat, N. Mazaki, S. Tsutsumi, T. Aizawa, Mater Trans 42 (2001) 1317–1321.
[60] H.R. Bakhsheshi-Rad, M.H. Idris, M.R. Abdul-Kadir, Surf. Coat. Technol. 222 (2013) 79–89.
[61] H.R. Bakhsheshi-Rad, E. Hamzah, A. Fereidouni-Lotfabadi, M. Daroonparvar, M.A.M. Yajid, M. Mezbahul-Islam, M. Kasiri-Asgarani, M. Medraj, Mater. Corros. 65 (2014) 1178–1187.
[62] A. Vinogradov, E. Merson, P. Myagkikh, M. Linderov, A. Brilevsky, D. Merson, Materials 16 (2023) 1324.
[63] S. Zhang, J. Li, Y. Song, C. Zhao, X. Zhang, C. Xie, Y. Zhang, H. Tao, Y. He, Y. Jiang, Y. Bian, Mater. Sci. Eng. C 29 (2009) 1907–1912.
[64] F. Witte, V. Kaese, H. Haferkamp, E. Switzer, A. Meyer-Lindenberg, C.J. Wirth, H. Windhagen, Biomaterials 26 (2005) 3557–3563.
[65] L. Scheideler, C. Füger, C. Schille, F. Rupp, H.P. Wendel, N. Hort, H.P. Reichel, J. Geis-Gerstorfer, Acta Biomater. 9 (2013) 8740–8745.
[66] A. Fazel Anvari-Yazdi, K. Tahermanesh, S.M.M. Hadavi, T. Talaei-Khozani, M. Razmkhah, S.M. Abed, M.S. Mohtasebi, Mater. Sci. Eng. C 69 (2016) 584–597.
[67] L. Mao, L. Shen, J. Chen, X. Zhang, M. Kwak, Y. Wu, R. Fan, L. Zhang, J. Pei, G. Yuan, C. Song, J. Ge, W. Ding, Sci. Rep. 7 (2017) 46343.
[68] Y. Li, X. Wang, J. Ren, X. Lan, J. Li, J. Yi, L. Liu, Y. Han, S. Zhang, D. Li, S. Lu, BMC Pharmacol. Toxicol. 18 (2017) 5, doi:10.1186/s40360-016-0113-6.
[69] J. Sugimoto, A.M. Romani, A.M. Valentin-Torres, A.A. Luciano, C.M. Ramirez Kitchen, N. Funderburg, S. Mesiano and H.B. Bernstein, *J. Immunol.*, 2012, 188, 6338–6346.
[70] F. da S. Lima, R.A. Fock, Int. J. Mol. Sci. 21 (2020) 1–22.
[71] M. Bessa-Gonçalves, C. Ribeiro-Machado, M. Costa, C.C. Ribeiro, J.N. Barbosa, M.A. Barbosa, S.G. Santos, Acta Biomater. 155 (2023) 667–683.